Nanoscale

PAPER

Check for updates

Femtosecond-laser-patterned origami Janus membrane toward enhanced water fog harvesting†

YanSheng Yao,[a] Tao Peng,[a] Yubin Peng,[a] Qiangsong Meng,[a] Suwan Zhu, [ID] *[b] Yanlei Hu, [ID][b] Jiawen Li [ID][b] and Dong Wu [ID][b]

Fog harvesting is an effective way to relieve water shortages in arid regions; thus, improving the efficiency of fog harvesting is urgently needed for both academic research and practical applications. Here, we report an origami patterned Janus (O-P-Janus) membrane using laser-ablated copper foams inspired by origami handcraft and traditional Chinese architecture. Compared to the planar fully ablated Janus membrane, our O-P-Janus membrane, with selectively ablated rectangular areas, exhibits an exceptional water collection rate (WCR) of approximately 267%. The underlying physical mechanism of WCR enhancement is revealed and attributed to the enhanced fog adsorbing capacity on the upper superhydrophobic origami structures and the accelerated removal of accumulated droplets beneath the lower superhydrophilic V-shaped tips. This O-P-Janus membrane with excellent fog collection performance should open up a new avenue for both device designs and potential applications toward structuring-enhanced fog collection and microfluidic control platforms.

1. Introduction

As global warming intensifies, recent decades have witnessed a serious rise in the levels of water scarcity worldwide. Unfortunately, the severe pollution and uneven distribution of freshwater resources have placed a heavier burden on arid areas. Therefore, there is an urgent need to develop highly efficient and eco-friendly approaches to freshwater harvesting.[1–3] Researchers have reported diverse materials/methods for freshwater collection to meet a wide variety of usage scenarios such as osmotic membranes,[4] sewage treatment,[5] desalination,[6] fog collection,[7] *etc*. It should be emphasized that water fog is composed of a large number of tiny water droplets suspended in the atmosphere, which constitutes approximately 10% of freshwater resources on Earth.[8] Hence, fog collection is considered to be a very promising and low-cost remedy for alleviating global water shortages.

During long biological evolution, creatures in nature have evolved a wide variety of superior fog collection abilities to survive.[9] For instance, desert beetles can effectively harvest and transport tiny water drops in the air using protrusion structures on their backs.[10] Cacti can collect water from moist air using conical spines on their surfaces.[11,12] Spiders can capture water using their asymmetric patterned webs.[13] Inspired by these examples, corresponding bionic fog collection systems have been designed such as hydrophilic/hydrophobic protrusion surfaces,[14–16] needle-shaped arrays,[17–23] and spider silk-like nanofiber swelling structures.[24–27] As a typical self-driven water collection platform without power input, the Janus membrane with asymmetric structures/wettability on two opposite sides has proven its great potential in efficient and low-cost liquid/gas collection scenarios.[28–32] However, most traditional Janus membranes are based on planar frameworks with uniform wettability or patterns on a single side; thus, water fog cannot be captured and separated selectively at the interfaces, thus leading to a low water collection efficiency. To address this issue, two key metrics should be taken into consideration for the improvement of Janus membranes: (1) high fog adsorption rate on the surface and (2) rapid water infiltration and detachment.

Inspired by the excellent water collection and drainage properties on corrugated cardboard-shaped structures from traditional Chinese roof tile architectures, we adopted an origami craft to fabricate a three-dimensional (3D) O-P-Janus membrane *via* selective femtosecond laser processing and compression molding of 3D printing technology,[33,34] to create asymmetric wettability gradients across the thickness as well as on the bottom of porous copper foam. Compared to the

[a]*Intelligent Manufacturing Laboratory, School of Mechanical and Electrical Engineering, Anhui Jianzhu University, Hefei 230009, China.*
E-mail: suwanzhu@ustc.edu.cn
[b]*CAS Key Laboratory of Mechanical Behavior and Design of Materials, Key Laboratory of Precision Scientific Instrumentation of Anhui Higher Education Institutes, Department of Precision Machinery and Precision Instrumentation, University of Science and Technology of China, Hefei 230026, China*
†Electronic supplementary information (ESI) available. See DOI: https://doi.org/10.1039/d3nr03829g

planar fully-ablated Janus membrane, this O-P-Janus membrane with optimized rectangular patterns exhibited an exceptional WCR of up to ~267%. The impact of diverse parameters, including side length, vertex angle and patterning length ratio on WCR, was systematically studied. The basic physics behind the WCR enhancement is attributed to the enhanced fog adsorbing capacity on the upper origami structures and the rapid removal of accumulated droplets on the laser-patterned superhydrophilic bottom. This O-P-Janus membrane with enhanced water collection performance should offer a promising alternative for both device designs and practical applications toward efficient water harvesting platforms and microfluidic manipulation.

2. Results and discussion

Commercially available copper foam (thickness ~0.5 mm, 130 PPI) was chosen as the substrate of the Janus membrane because of its larger specific surface area compared to traditional planar Janus membranes. The pristine copper foam plates showed a water contact angle (WCA) of ~108° after ultrasonic cleaning in alcohol and deionized water. The cleaned samples were modified by Glaco chemical spray and showed superhydrophobicity with a WCA of ~155°. Then, the superhydrophobic copper foam was selectively patterned by femtosecond laser line-by-line fast scanning on a single side to form the patterned Janus copper foam with a WCA of ~0° on the laser-treated surface. In the last step, the O-P-Janus was formed by mechanical folding through 3D-printed molds [Fig. 1(a)]. The design of the O-P-Janus membrane is inspired by the origami handcraft and traditional Chinese architectural roof tile structures [Fig. 1(b)]. The folded and inclined surface

(fully superhydrophobic) induces the spontaneous directional movement of water droplets on the upper side, while the wetting gradient across the thickness allows the droplets to efficiently transport from the superhydrophobic side to the partially-hydrophilic patterned side through the internal micropores. The selective penetration of the water droplets was observed from the laser-untreated side to the other side, but a blockage occurred from the opposite direction [Fig. 1(c) and Movie S1 in ESI†]. With the resultant gravitational force and wetting gradient force, the 3D O-P-Janus possesses an enhanced capability for water fog collection.

The surface morphology and element analysis of O-P-Janus were then characterized. As shown in Fig. 2(a), the yellowish-brown area denotes the Glaco-modified copper foam, and the black area is the femtosecond laser-ablated area. The magnified scanning electron microscopy (SEM) images indicate a uniform shell formed on the branches of the copper foam due to the superhydrophobic SiO_2 nanoparticle coatings [Fig. 2(b)]. It should be noted that the pristine copper frame was basically preserved after femtosecond laser ablation [Fig. 2(c)], but the superhydrophobic SiO_2 shell was destroyed by the high-energy laser ablation, which is evidenced by the coverage of the scattered nanoparticles in different forms on the hollow branches of the copper foam [Fig. 2(d)], as well as the element analysis in Fig. 2(e). Energy-dispersive X-ray spectroscopy (EDS) shows that the atomic proportions of O, Si, and Cu elements in the pristine copper foam were 5.47%, 0.09%, and 94.44%, respectively, indicating the major element of pure copper. Because the Glaco chemical coating contains silica nanoparticles, the proportion of elements O and Si increased sharply to 36.75% and 16.22%, respectively, in the superhydrophobic copper foam. Accordingly, the percentage of elemental Cu decreased to 47.03%. Compared with the superhydrophobic copper
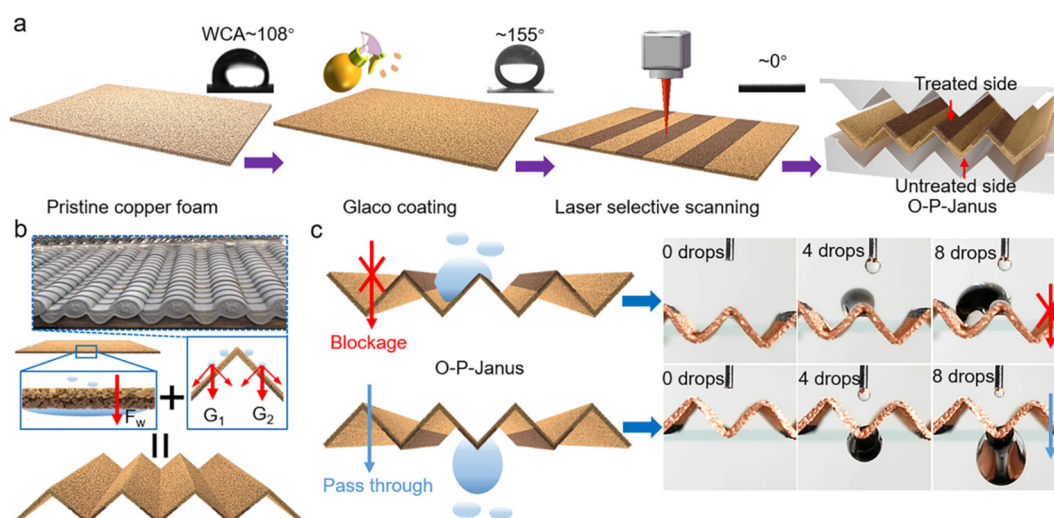
Fig. 1 Fabrication, design inspiration and unidirectional water penetration behavior of O-P-Janus copper foam. (a) Three-step fabrication of O-P-Janus includes superhydrophobic coating, selective laser patterning, and mechanical folding using 3D printed molds. (b) The platform design is inspired by origami handcraft and traditional Chinese architectural roof tiles. (c) Spontaneous and unidirectional penetration of droplets from the superhydrophobic side to the laser-treated side.
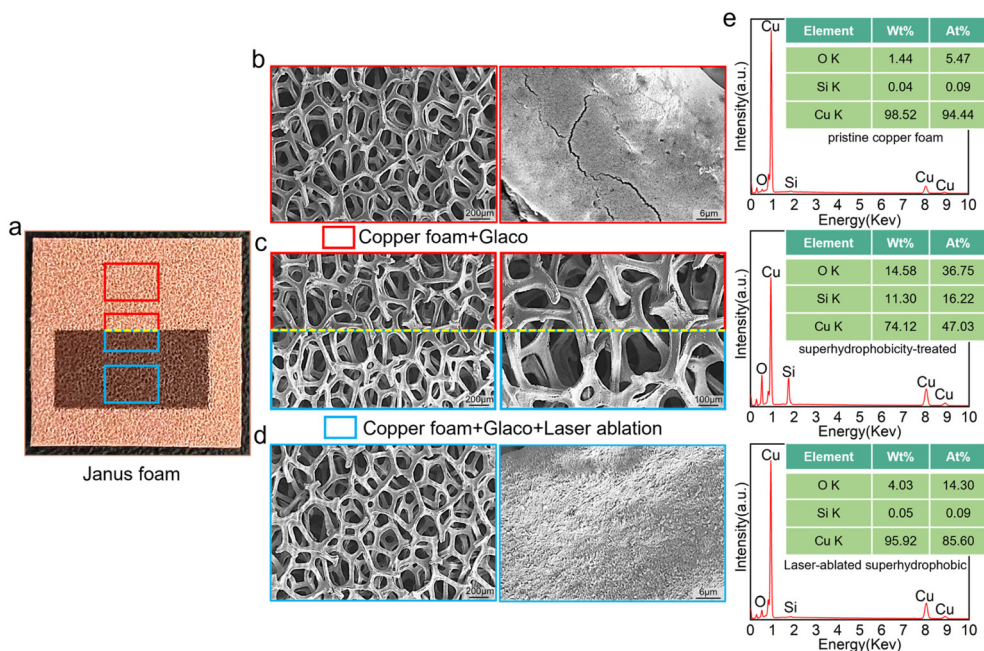
Fig. 2 SEM images and EDS elemental analysis. (a) The optical photograph of a typical O-P-Janus. (b–d) SEM images of different areas on the O-P-Janus. The red box denotes the Glaco-treated copper foam and the blue box denotes the laser-ablated sample in the red box. The yellow dotted line gives the interface of the two surfaces. (e) EDS element analysis for O-P-Janus at different fabrication stages: pristine copper foam, superhydrophobic copper foam, and laser-ablated superhydrophobic copper foam.

foam, the laser-ablated sample showed a decrease in the elements O and Si by 22.45% and 16.13%, respectively. The percentage of O was still slightly greater than that in the pristine sample, but the Si content remained the same, which demonstrated the complete removal of the silica coatings and the mild oxidation on the copper foam surface after femtosecond laser ablation.

The fog collection experiments of the Janus membranes were performed on a homemade fog-generating platform [Fig. 3(a)]. A planar patterned Janus membrane was fixed at a vertical distance of ~10 cm below the humidifier fog outlet. The dynamic fog flow was characterized using a high-speed camera at 200× slow motion (Fig. S1 and Movie S2, ESI†). It is observed that a tiny, stable and uniform fog flow formed after $t = 50$ ms. The humidifying capacity, *i.e.*, the generated fog volume per hour, was quantified and is shown in Fig. 3(b). By calculating the average weight loss of the humidifier for one hour, the humidifying capacity was stabilized at 370 mL h^{-1} within half a day, indicating the favorable fog-generating sustainability of this platform. The impacts of laser power and scanning speed on the WCR are shown in Fig. 3(c) and (d) and the corresponding morphology evolutions are found in Fig. S2, ESI.† It is observed that a laser power within the range of 200–400 mW exhibited better WCRs of ~0.75 g cm^{-2} h^{-1}, and a scanning speed within the range of 4–6 mm s^{-1} had better WCRs. Other typical processing parameters, such as patterning period, scanning width and mode, are shown in Fig. S3 and S4 in the ESI.† It is observed that a smaller processing width and a vertically crossed line-by-line laser scanning mode exhibited

a better WCA, which could be attributed to the more intensive and uniform laser ablation on the copper branches. It should be noted that a full modification of wettability for base materials is beneficial for a better water harvesting performance for Janus-type devices. Taking into account both laser fabrication efficiency and WCRs, the laser processing parameters were used with laser power = 300 mW, scanning width = 60 μm and scanning speed = 6 mm s^{-1} throughout the experiments.

The superiority of the elaborately-designed O-P-Janus in the water collection scenario was evidenced by the following comparison experiments [Fig. 4(a) and (b)], where six typical configurations were employed in the same projected area (25 × 25 mm^2): double-sided fully laser-ablated planar copper foam (DFLPC), single-sided fully laser-ablated planar pristine copper foam (SFPPC), single-sided fully laser-ablated planar superhydrophobicity-treated copper foam (P-Janus), origami-structured P-Janus (O-Janus) (vertex angle 60°, origami-structured side length 5 mm), P-Janus with single-sided partially laser-ablated patterns (P-P-Janus) and O-Janus with single-sided partially laser-ablated patterns (O-P-Janus). The DFLPC exhibited a significantly lower WCA compared to the typical superhydrophobic-superhydrophilic Janus. Interestingly, the WCR of O-P-Janus reached an extremum of approximately 1.47 g cm^{-2} h^{-1}, significantly higher than those of the other four configurations, indicating that the synergy of origami structures and the selective laser-ablated patterns was beneficial for improving the WCR for the planar Janus devices. Typically, P-P-Janus showed a decreased WCA of ~0.78 g cm^{-2} h^{-1} compared with
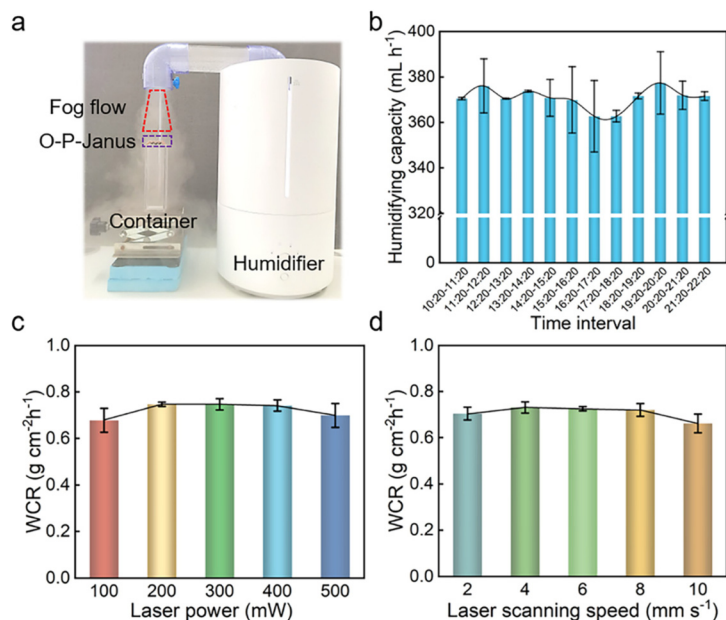
Fig. 3 The fog collection platform and impact of laser processing parameters on WCR. (a) A homemade fog collection device consisting of a lifting platform, a container and a humidifier. (b) The humidifying capacity was stabilized at 370 mL h^{-1} within half a day, indicating the favorable fog-generating sustainability of this platform. Impacts of (c) laser processing power and (d) laser scanning speed on WCA for Janus membranes.

that of O-P-Janus, which might suggest the WCR-enhancing effect of the origami structures. Counterintuitively, the WCR of O-Janus was only ~0.62 g cm^{-2} h^{-1}, which was 0.1 g cm^{-2} h^{-1} lower than that of P-Janus. These results indicate that the mere increase in specific surface area, *i.e.*, the introduction of origami structures, may not improve the water collection efficiency for planar Janus membranes. In Fig. 4(c), the relation between the vertex angle of O-Janus and WCA was given, in which only 30°- and 90°-O-Janus reached almost the same WCA of 0.72 g cm^{-2} h^{-1} as that of P-Janus. The minimum WCR of ~0.57 g cm^{-2} h^{-1} was found at a vertex angle of 45°.

Further, the influence of diverse geometric parameters of O-P-Janus on the WCR was investigated, including the vertex angle, origami-structured side length and patterning ratio, which are clearly defined in Fig. 4(d)–(f). Compared to O-Janus, the WCRs of O-P-Janus were always greater than those at the same angles, showing a maximum variance of ~1.07 g cm^{-2} h^{-1} and a minimum variance of ~0.31 g cm^{-2} h^{-1}. When the vertex angle was set to 90°, the WCA of O-P-Janus reached a maximum value of 1.79 g cm^{-2} h^{-1} [Fig. 4(d)], side length = 5 mm and patterning ratio = 4 : 4. The relation between the side length and WCR of O-P-Janus is revealed in Fig. 4(e), in which the vertex angle and patterning ratio were fixed at 90° and 4 : 4, respectively. The maximum WCA reached ~1.92 g cm^{-2} h^{-1} when the side length was 4 mm. In Fig. 4(f), we investigated one of the most important metrics, *i.e.*, the laser patterning ratio, which impacts on the WCA. The vertex angle and side length were fixed at 90° and 4 mm, respectively. The laser patterning ratio is defined as $a : b$, where a denotes the width of the laser-ablated rectangle and b is the width of the

adjacent non-ablated rectangle. The maximum WCR of ~1.92 g cm^{-2} h^{-1} was observed when $a : b$ = 4 : 4. While the proportion of laser-ablated area $(a : b)$ increased, the WCA declined sharply. In the case of $a : b$ = 6 : 2, the WCA was almost reduced by half compared to the maximum. In an extreme case of $a : b$ = ∞ (*i.e.*, O-Janus), the WCR of O-Janus was only ~0.62 g cm^{-2} h^{-1}. Note that O-P-Janus with optimized parameters manifested a significantly enhanced WCR of ~267% compared to that of P-Janus, showing its superiority in efficient water collection.

We also briefly explored the influence of the laser-ablated pattern shapes on the WCA for O-P-Janus. Diamond-like origami-structured patterns were fabricated [Fig. 4(g)]. The length of each diamond was the same as the rectangles on the O-P-Janus, and the width was determined by the number of close-packed diamonds on the Janus membrane. When the number of diamonds was small (3), the WCA of the variant O-P-Janus was relatively low, only approximately 1.05 g cm^{-2} h^{-1}. Once the diamond number increased to 12, the WCA increased to ~1.36 g cm^{-2} h^{-1}. The WCR remained stable as the diamond number continued increasing to 30. Despite its considerable WCR increase of up to 89% compared to P-Janus, O-P-Janus with periodic rectangle patterns showed an overwhelming increase of ~167% in WCR. A long-term stability test for a fresh O-P-Janus was performed [Fig. S4(d), ESI†]. It was observed that the WCA declined significantly within first three days and then became stable within the next five days. This is probably induced by surface oxidation, impurities adsorption and coating loss. Quickly drying and preserving in a sealed and clean environment after use should delay this phenomenon.
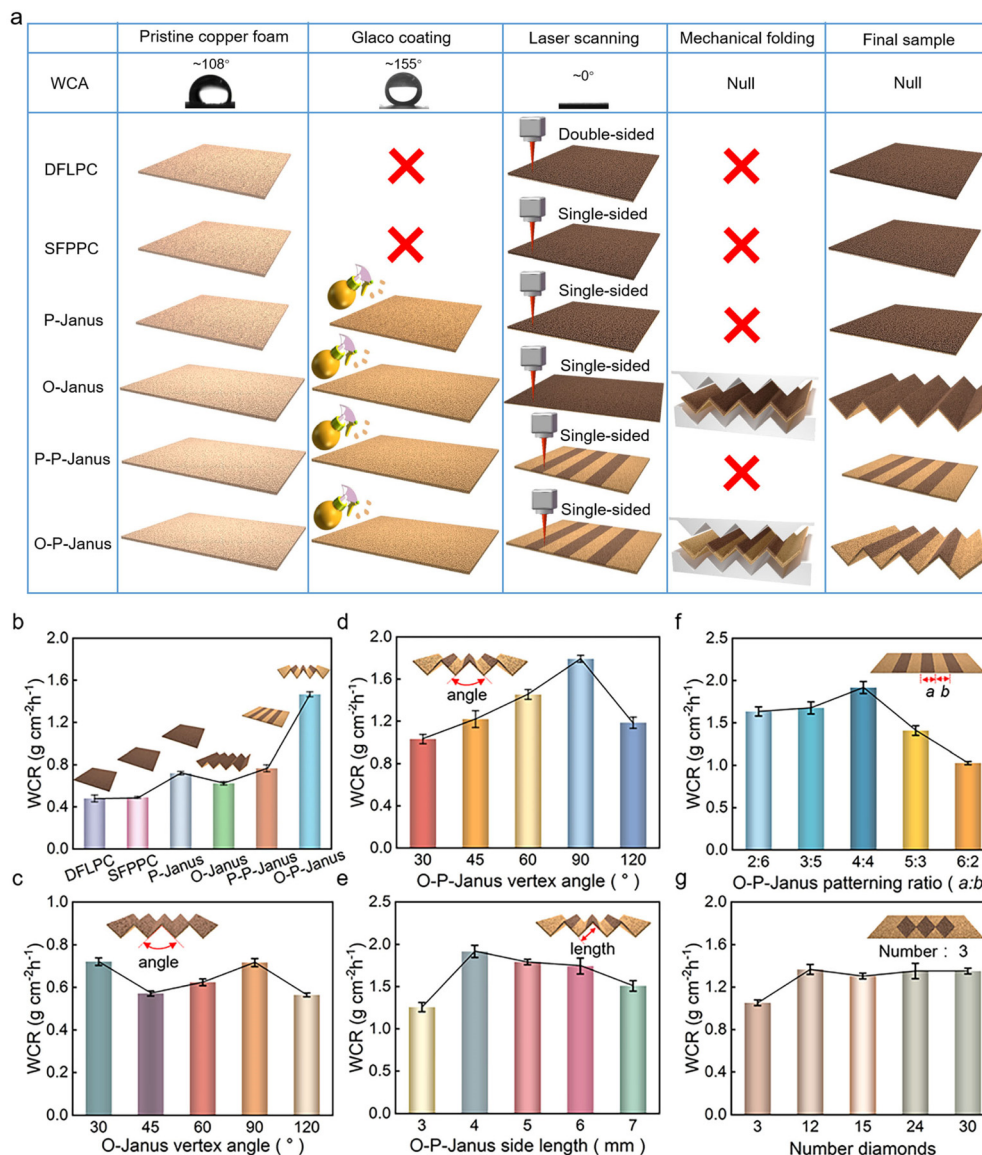
Fig. 4 (a) A schematic fabrication diagram for all the specimens. (b) A comparison experiment of WCA for six typical samples. (c) The effect of vertex angles of O-Janus on WCA. The impact of (d) vertex angle, (e) side length and (f) laser-ablated patterning ratio of O-P-Janus on WCR. (g) The effect of different numbers of diamond patterns on WCR in a variant O-P-Janus.

To elucidate the basic physics inside the intriguing enhancement of O-P-Janus configurations in water collection, the interfacial dynamics of fog harvesting were visualized at different typical stages using time-lapse photography, followed by force analysis. Five typical stages during water fog harvesting were observed in Fig. 5a(i)–a(v): fog capturing ($t = 1$ min 55 s), condensing ($t = 5$ min 39 s), penetrating ($t = 10$ min 54 s), growing ($t = 15$ min 54 s) and dripping ($t = 16$ min 48 s). Specifically, when the tiny fog droplets initially made contact with the upper superhydrophobic origami structures, they slowly condensed and gradually grew. Once the gravitational forces of the droplets, *i.e.*, the droplet volumes, were large enough, they rolled down into the valley of the origami structure, followed by rapidly penetrating the thickness of the copper foam and growing up

beneath the opposite superhydrophilic patterns. Detachment occurred as the gravitational forces of the droplets on the lower surface were greater than the capillary forces from the superhydrophilic patterns (Movie S3, ESI†). Fig. 5a(vi)–a(ix) show the time-lapse evolution of one droplet after penetrating the Janus membrane from different views.

As mentioned earlier, the enhancement of the water collection efficiency in Janus membranes relies on two crucial metrics: (1) a high fog adsorption rate on the surface and (2) rapid water penetration and detachment. Fig. 5(b) experimentally proved the superiority of O-P-Janus with an improved fog collection weight of 135.67 mg on the upper surface at an initial stage (first 180 s). For its planar counterpart, P-P-Janus showed a much lower fog collection weight of 80 mg.
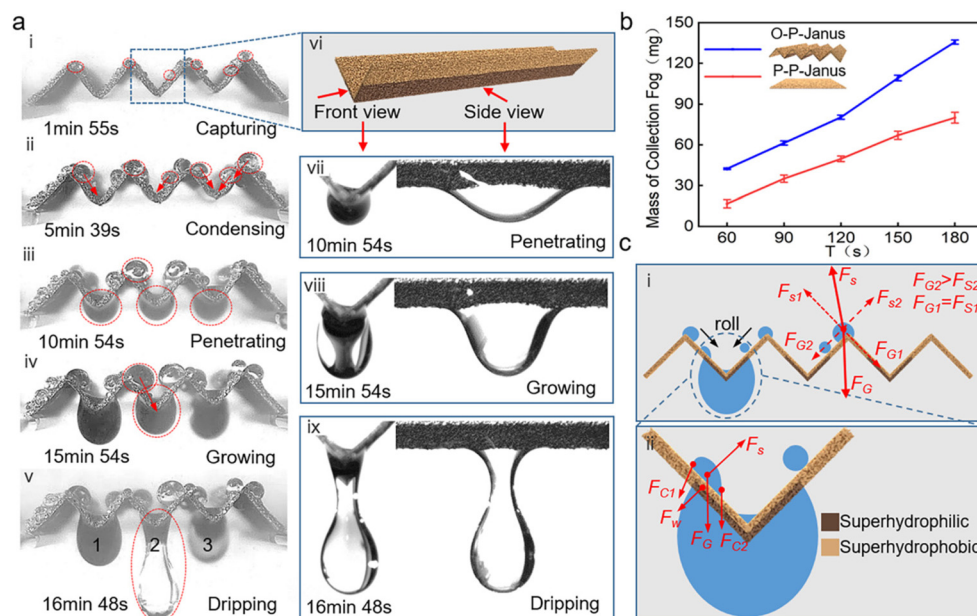
Fig. 5 Interfacial dynamics of the fog harvesting process and force analysis. (a) Time-lapse snapshots for typical stages during water harvesting processes: fog capturing, condensing, penetrating, growing and dripping. (b) Early-stage fog collection efficiency on the upper surfaces of O-P-Janus and P-Janus. (c) Force analysis of water collection at later stages on a quadruple-folded origami structure.

Naturally, an origami structure has a higher water adsorption rate on the surface because of its larger specific surface area. Force analysis was subsequently performed to understand the penetration and detachment behaviors of the drops [Fig. 5(c)]. Taking a leftward rolling droplet as an example on the roof, once the component of the gravitational force F_{G2} exceeds the

Table 1 A comparison between O-P-Janus and recently-reported water harvesting devices

Platform type	Driving principle	Motion directivity	Sample fabrication	Fog flow	Collection efficiency	Advantages
SHB/SHL/SHB[35]	Gravitational force	Penetrating & dripping	Chemical processing	Velocity ~100 cm s^{-1}	~370 mg cm^{-2} h^{-1}	Collection free direction
Fog Harps[36]	Gravitational force Elastocapillary force	Unilateral sliding	Stretching steel string	0.69 to 4.17 g min^{-1} per humidifier, clusters were used	$\eta \approx 17\%$	Low cost, easy fabrication for larger areas
Polycarbonate fibers[37]	Electric potential gradient	Unilateral sliding	Chemical processing	Velocity ~19 cm s^{-1}	~75 mg cm^{-2} h^{-1}	Strong and fast absorption
Spine with barbs and hierarchical channels[20]	Capillary force Laplace pressure gradient	Unilateral sliding	Laser fabrication + chemical processing	Velocity ~25–30 cm s^{-1} RH ~90%	~560 mg cm^{-2} h^{-1}	Low cost, strong driving force and high-efficient
Curved inclined arc-pitted grooves[38]	Gravitational force Laplace pressure gradient Capillary force	Unilateral sliding	3D printing	RT ~25 °C RH ~75% RT ~25 °C	~109 ± 25.4 mg h^{-1}	Easy fabrication
Beetle and cactus-inspired surfaces[39]	Gravitational force Laplace pressure gradient	Unilateral sliding	Chemical processing + standard photolithography + deep reactive ion etching	Velocity ~60–70 cm s^{-1} RH ~80 ± 5% RT ~20 ± 3 °C	~119 mg cm^{-2} h^{-1}	Long-range transport droplet
O-P-Janus (This work)	Gravitational force Wetting gradient force Capillary force	Penetrating & dripping	Laser fabrication + 3D printing	Flux ~370 mL h^{-1}	~1917.1 mg cm^{-2} h^{-1}	High efficiency, generalized enhancement for 2D platforms

component of the support force F_{S2} along the slope, the droplet rolls downward along the groove and grows up [Fig. 5c (i)]. Four external forces acted on the droplet when it reaches the opposite of the superhydrophilic pattern, which are the gravitational force F_G, the asymmetric capillary forces F_{C1} and F_{C2}, the wetting gradient force F_w, and the support force F_S [Fig. 5c(ii)]. The positive force is defined as the resultant force of F_G, F_w and F_C along the penetrating direction, which promotes the penetration of droplets. For a droplet of the same size, the inclined origami structure leads to an enlarged penetration depth and a decreased positive force. To a certain extent, it should slow the water-penetrating process. Due to the overwhelming wetting gradient force along the vertical direction for Janus-type devices, the water penetration time is usually very short (<1 s) compared to its detachment time (usually tens of minutes).

In the detachment process, the pendent water droplets accumulated on the bottom of O-P-Janus and rapidly pinched off at the V-shaped end with thin necks. In contrast, the accumulated droplets beneath P-P-Janus slowly pinched off in flat areas with thick necks [Fig. 5a(ix) and Movie S4 in ESI†]. That is, O-P-Janus accelerates the removal process of the collected droplets at the V-shaped tips. However, the bottom of P-P-Janus is gradually covered by flat water layers during the fog capturing process due to a larger interfacial adhesion force between water and the superhydrophilic solid wall. Going back to Fig. 4(a), P-Janus showed a slightly lower WCR than P-P-Janus, which also suggested that the introduction of selective laser ablation could accelerate the removal of water droplets on a planar surface. A detachment time delay of approximately 7 minutes was observed between P-P-Janus and quadruple-folded O-P-Janus, which proved the superiority of O-P-Janus in rapid water detachment (Movie S3†). Hence, compared to other recently-reported devices (Table 1), the synergy of the origami framework and the selective laser-ablated patterns promotes the fog adsorption rate and rapid water detachment at the heterointerface, exhibiting an exceptional water collection efficiency of approximately 1917.1 mg cm^{-2} h^{-1}. Besides, this O-P-Janus also provides a generic integrated solution to the water collection enhancement for current 2-D Janus platforms.

3. Conclusions

To conclude, inspired by origami handcraft and traditional Chinese roof tile structures, a 3D O-P-Janus membrane was designed and fabricated by selectively ablating porous copper foam through high-precision femtosecond laser processing and 3D-printed compression molding technologies. The impact of diverse parameters of O-P-Janus on WCR, including side length, vertex angle, and patterning length ratio, was further quantified to achieve optimized device performance. The selective laser-ablated patterns and wettability gradient on O-P-Janus greatly enhanced the WCR to ~267% compared to a planar fully-patterned Janus membrane. By using time-lapse photography of the fog collection process, the underlying

mechanism of WCR enhancement in O-P-Janus was elucidated, which stemmed from the enhanced fog adsorbing capacity on the upper origami roof and the fast detachment of the adsorbed water beneath the V-shaped superhydrophilic patterns. This structure-enhanced O-P-Janus membrane should facilitate the current designs in efficient fog collection systems as well as microfluidic manipulation.

4. Materials and methods

4.1. Preparation and modification of the samples

Commercially- available copper foams ($25 \times 25 \times 0.5$ mm^3, 130 PPI) were ultrasonicated in alcohol and deionized water baths for 5 minutes. The cleaned samples were coated with commercial Glaco Mirror Coat Zero (SOFT99, Japan) to endow them with superhydrophobicity properties. A laser beam generated by a regenerative-amplified Ti: sapphire femtosecond laser system (Legend Elite-1K-HE, Coherent, 104 fs, 1 kHz, 800 nm) was used for selective laser patterning on the superhydrophobic copper foam to form planar Janus membranes. The laser beam passed a computer-controlled high-speed galvanometer scanner (SCANLAB, Germany) and focused on the sample surface (spot diameter ~20 μm) through the telecentric f–θ lens (focal length of 63 mm). Specifically, the desired patterns with periodic structures were first drawn by AutoCAD software and then imported into the control program of the galvanometer scanner (CSMark). Afterward, the O-P-Janus was fabricated *via* compression using 3D-printed layer-by-layer stacking molds.

4.2. Characterization

WCAs were measured with a volume = 5 μL droplet using a contact angle measurement system (CA100D, Innuo, China) five times at different sites to calculate the average value. The surface morphology was characterized by a field-emission scanning electron microscope (JSM-6700F, JEOL, Japan). A humidifier (MJJSQ05DY, China) was used to generate stable water fog at an average humidifying rate of 370 mL h^{-1}. A high-resolution CCD camera (WP-GUT030M, Huagu Power Tech., China) was used to observe and record the dynamic water collection process for fog/droplets.

4.3. Fog collection experiments

The samples were fixed at a vertical distance of ~10 cm below the outlet of a homemade fog generating system. WCRs of different samples were calculated by the container weight variation before/after water collection *versus* the effective areas of each sample.

Author contributions

YanSheng Yao and Suwan Zhu conceived the idea. Tao Peng and Suwan Zhu wrote the manuscript text and designed the experimental device. Suwan Zhu and Tao Peng performed the experiments. Yubin Peng and Qiangsong Meng provided

assistance in data analysis and characterization. Yanlei Hu, Jiawen Li and Dong Wu provided equipment and manuscript revision. All authors reviewed the manuscript.

Conflicts of interest

There are no conflicts to declare.

Acknowledgements

References

1 B. I. Cook, J. E. Smerdon, R. Seager and E. R. Cook, *J. Clim.*, 2014, **27**, 383–397.

2 J. Eliasson, *Nature*, 2015, **517**, 6.

3 M. M. Mekonnen and A. Y. Hoekstra, *Sci. Adv.*, 2016, **2**, e1500323.

4 L. F. Greenlee, D. F. Lawler, B. D. Freeman, B. Marrot and P. Moulin, *Water Res.*, 2009, **43**, 2317–2348.

5 Y. P. Chen, C. Wu, W. X. Ma, Y. Li and Y. Chen, *Adv. Mater. Res.*, 2013, **726**, 2576–2579.

6 Y. Zhu, G. Tian, Y. Liu, H. Li, P. Zhang, L. Zhan, R. Gao and C. Huang, *Adv. Sci.*, 2021, **8**, 2101727.

7 K. Zhang, H. Chen, T. Ran, L. Zhang, Y. Zhang, D. Chen, Y. Wang, Y. Guo and G. Liu, *ACS Appl. Mater. Interfaces*, 2022, **14**, 33993–34001.

8 O. Klemm, R. S. Schemenauer, A. Lummerich, P. Cereceda, V. Marzol, D. Corell, J. Van Heerden, D. Reinhard, T. Gherezghiher and J. Olivier, *Ambio*, 2012, **41**, 221–234.

9 H. Zhu, Z. Guo and W. Liu, *Chem. Commun.*, 2016, **52**, 3863–3879.

10 A. R. Parker and C. R. Lawrence, *Nature*, 2001, **414**, 33–34.

11 J. Ju, H. Bai, Y. Zheng, T. Zhao, R. Fang and L. Jiang, *Nat. Commun.*, 2012, **3**, 1247.

12 Y. Xiao and Z. Guo, *New J. Chem.*, 2021, **45**, 21125–21150.

13 Y. Zheng, H. Bai, Z. Huang, X. Tian, F.-Q. Nie, Y. Zhao, J. Zhai and L. Jiang, *Nature*, 2010, **463**, 640–643.

14 Y. Hou, M. Yu, X. Chen, Z. Wang and S. Yao, *ACS Nano*, 2015, **9**, 71–81.

15 W. Huang, X. Tang, Z. Qiu, W. Zhu, Y. Wang, Y.-L. Zhu, Z. Xiao, H. Wang, D. Liang and J. Li, *ACS Appl. Mater. Interfaces*, 2020, **12**, 40968–40978.

16 E. Kostal, S. Stroj, S. Kasemann, V. Matylitsky and M. Domke, *Langmuir*, 2018, **34**, 2933–2941.

17 H. Bai, T. Zhao, X. Wang, Y. Wu, K. Li, C. Yu, L. Jiang and M. Cao, *J. Mater. Chem. A*, 2020, **8**, 13452–13458.

18 J. Ju, K. Xiao, X. Yao, H. Bai and L. Jiang, *Adv. Mater.*, 2013, **25**, 5937–5942.

19 Y. Shi, O. Ilic, H. A. Atwater and J. R. Greer, *Nat. Commun.*, 2021, **12**, 2797.

20 J. Wang, S. Yi, Z. Yang, Y. Chen, L. Jiang and C.-P. Wong, *ACS Appl. Mater. Interfaces*, 2020, **12**, 21080–21087.

21 T. Xu, Y. Lin, M. Zhang, W. Shi and Y. Zheng, *ACS Nano*, 2016, **10**, 10681–10688.

22 S. Yi, J. Wang, Z. Chen, B. Liu, L. Ren, L. Liang and L. Jiang, *Adv. Mater. Technol.*, 2019, **4**, 1900727.

23 H. Zhou, M. Zhang, C. Li, C. Gao and Y. Zheng, *Small*, 2018, **14**, 1801335.

24 H. Bai, J. Ju, R. Sun, Y. Chen, Y. Zheng and L. Jiang, *Adv. Mater.*, 2011, **23**, 3708–3711.

25 H. Bai, X. Tian, Y. Zheng, J. Ju, Y. Zhao and L. Jiang, *Adv. Mater.*, 2010, **22**, 5521–5525.

26 J. Knapczyk-Korczak and U. Stachewicz, *Nanoscale*, 2021, **13**, 16034–16051.

27 Y. Liu, N. Yang, C. Gao, X. Li, Z. Guo, Y. Hou and Y. Zheng, *ACS Appl. Mater. Interfaces*, 2020, **12**, 28876–28884.

28 X. Zeng, W. Zhou, P. Zhou, M. Zhang, C. Zhou, L. Tan and L. Wang, *J. Environ. Chem. Eng.*, 2021, **9**, 105325.

29 L. Zhong, J. Feng and Z. Guo, *J. Mater. Chem. A*, 2019, **7**, 8405–8413.

30 W. Zhou, C. Zhou, H. Yang, J. Wang, J. Du, L. Chen, H. Shen, L. Tan, L. Dong and X. Zeng, *J. Environ. Chem. Eng.*, 2021, **9**, 105899.

31 R. Zhu, M. Liu, Y. Hou, L. Zhang, M. Li, D. Wang, D. Wang and S. Fu, *ACS Appl. Mater. Interfaces*, 2020, **12**, 50113–50125.

32 S. Zhu, J. Li, S. Cai, Y. Bian, C. Chen, B. Xu, Y. Su, Y. Hu, D. Wu and J. Chu, *ACS Appl. Mater. Interfaces*, 2020, **12**, 18110–18115.

33 K. T. Zhang, H. W. Chen, T. Ran, L. W. Zhang, Y. Zhang, D. K. Chen, Y. Wang, Y. R. Guo and G. Liu, *ACS Appl. Mater. Interfaces*, 2022, **14**, 33993–34001.

34 S. Zhu, Y. Bian, T. Wu, E. Li, J. Li, Y. Hu, D. Wu and J. Chu, *Appl. Phys. Lett.*, 2020, **116**, 093706.

35 J. Li, W. Li, X. Han and L. Wang, *J. Colloid Interface Sci.*, 2021, **581**, 545–551.

36 J. Kaindu, K. Murphy, N. Kowalski, A. Jones, M. Fleming, B. Kennedy and J. Boreyko, *Droplet*, 2023, e78.

37 D. Ura, J. Knapczyk-Korczak, P. Szewczyk, E. Sroczyk, T. Busolo, M. Marzec, A. Bernasik, S. Kar-Narayan and U. Stachewicz, *ACS Nano*, 2021, **15**, 8848–8859.

38 L. Liu, S. Liu, M. Schelp and X. Chen, *ACS Appl. Mater. Interfaces*, 2021, **13**, 29122–29129.

39 X. Wang, J. Zeng, J. Li, X. Yu, Z. Wang and Y. Zhang, *J. Mater. Chem. A*, 2021, **9**, 1507–1516.